ARTICLE

Check for updates

Coherent oscillation between phonons and magnons

Tomosato Hioki [1,2✉], Yusuke Hashimoto[1] & Eiji Saitoh[1,2,3]

Consider observing two different waves with the same frequency and wavelength. When these waves are coupled, the amplitude alternates between the two waves periodically, a phenomenon called coherent beating oscillation. Such phenomena can be seen in familiar coupled pendulums and, on a cosmic scale, neutrino oscillations: the oscillation between different types of neutrinos. In solids, on the other hand, there are various wave excitations responsible for their thermal and electromagnetic properties. Here we report the observation of coherent beating between different excitation species in a solid: phonons and magnons. By using time-resolved magneto-optical microscopy, magnons generated in $Lu_2Bi_1Fe_{3.4}Ga_{1.6}O_{12}$ gradually disappear by transforming to phonons, and after a while, they return to magnons. The period of the oscillation as a function of the field is consistent with the prediction of the magnon-phonon beating. The experimental results pave a way to coherent control of magnon-phonon systems in solids.

[1] Advanced Institute for Materials Research, Tohoku University, Sendai 980-8577, Japan. [2] Department of Applied Physics, Faculty of Engineering, University of Tokyo, Tokyo 113-8656, Japan. [3] Institute for AI and Beyond, The University of Tokyo, Tokyo 113-8656, Japan. ✉email: tomosato.hioki.d7@tohoku.ac.jp

Phonons refer to vibration waves of a crystal lattice in solids (Fig. 1a). They are responsible for the elastic and thermal properties of solids. On the other hand, magnons, or spin waves, refer to the wavy motion of magnetization in magnets, responsible for the magnetic and thermal properties (Fig. 1a)[1–5]. Phonons and magnons can interact in solids via the magneto-elastic and magnetostatic couplings[6–8] (Fig. 1b).

The dynamics of phonons and magnons in each system is written in their dispersion curves, curves that show the relation between the wavenumber and frequency. Figure 1c shows dispersion curves of transverse acoustic (TA) phonons and magnons in a film of typical magnetic insulator, lutetium iron garnet (LuIG)[9,10]. In the dispersion curves, the phonon dispersion and the magnon dispersion curves have an intersection, depicted as A in Fig. 1c, due to the magnetostatic gap in the magnon dispersion at $k = 0$. Around the intersection, a magnon-phonon hybridized state can be formed[11–14]. This state, called a magnon polaron, was experimentally found to exhibit extremely long lifetime, much longer than pure magnons, attributed to the hybridization with phonons with long lifetime[15,16]. In a lutetium iron garnet, the extended lifetime is confirmed by spin-heat conversion measurement even at room temperature[17]. As a result, when magnons are excited and sufficient time has passed, the pure magnons are attenuated, leaving magnon polarons. In magnon polarons, theoretically, the hybridization can cause level splitting, giving rise to an anti-crossing gap at the intersection in the dispersion curves, as shown in Fig. 1d. When the two states across the gap are excited simultaneously in a coherent way, coherent superposition of these two states, corresponding to beating oscillation between phonons and magnons, may be created (Fig. 1b).

We report the observation of coherent beating between phonons and magnons in lutetium iron garnet. By using time-resolved magneto-optical (TRMO) microscopy, we measured spatio-temporal magnetization dynamics, which couples with phonons in a thin film of lutetium iron garnet, LuIG. We found the coherent beating lasts up to tens of nanoseconds, which experimentally confirms strong coupling between magnons and phonons in the bare film of LuIG.

Results

Sample and measurement setup. To explore the beating oscillation in solids, we have developed TRMO microscopy. Figure 1e shows a schematic illustration of the experimental setup used in the present study. We used a thin film of $Lu_2Bi_1Fe_{3.4}Ga_{1.6}O_{12}$ (LuIG) with the thickness of 1.8 μm as a sample, exhibiting large magneto-optical effects[18,19] and small magnetization damping (See Supplementary Note 1). To excite magnetization dynamics, we focused a pulsed laser light (pump pulse) with the wavelength of 800 nm onto the sample, where the wavelength corresponds to almost half the energy of the bandgap of LuIG (~2.3 eV)[18,19]. The duration and the energy of the pulse is 100 fs and 1.0 μJ per pulse, respectively. The pump pulse excites spin waves, or magnons, via the photo-induced demagnetization and the photo-induced expansion effects[20–24]. We shaped the focus into a vertical line to selectively excite magnons with the wavevector **k** perpendicular to the vertical line (y axis) by using the Huygens-Fresnel interference[25]. Next, we shined another weak light pulse (probe pulse) with the wavelength of 630 nm (100 fs, 50 nJ per pulse) on the sample from the normal direction. We measured the spatial distribution of the magneto-optical Faraday rotation of the probe pulse transmitted through the sample by using a CCD camera (See Method for details)[26]. The Faraday rotation at each position on the sample $\theta_F(\mathbf{r}, t)$ reflects the local magnetization precession amplitude projected along the propagation direction of the probe pulse. By sweeping the time delay between the pump and probe
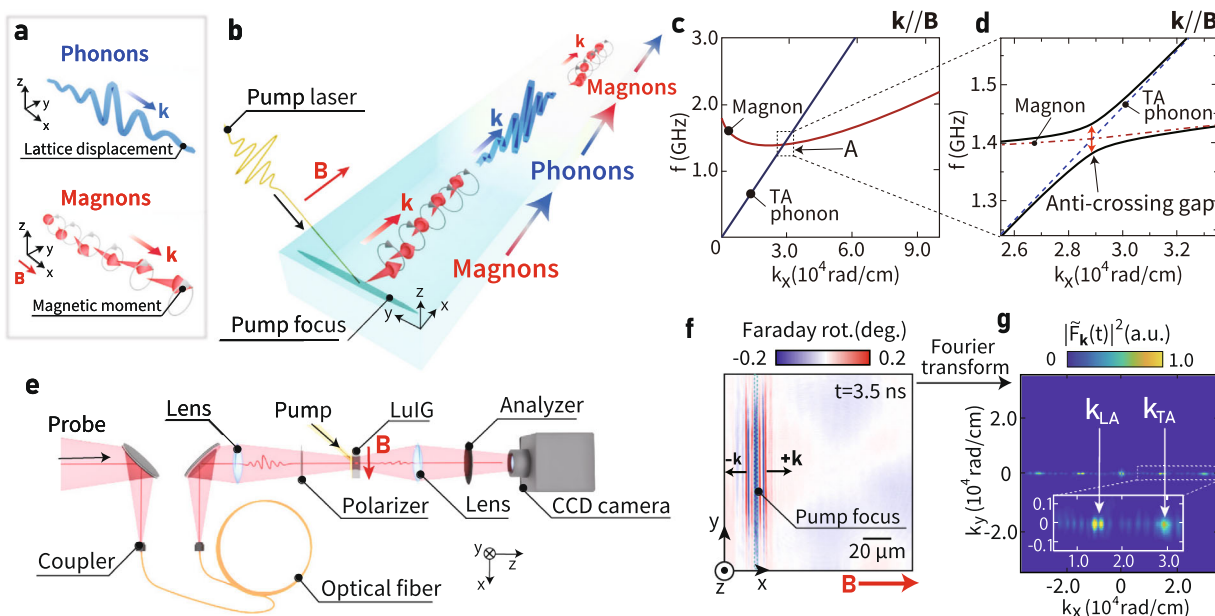
Fig. 1 Concept of coherent oscillation between phonons and magnons, and time-resolved magneto-optical microscopy. a A schematic illustration of phonons and magnons, **b** A schematic illustration of coherent oscillation between phonons and magnons. **c** The dispersion curves of phonon and magnon in lutetium iron garnet (LuIG). **d** A magnified view around A in Fig. 1c. The black curves represent the dispersion relation of hybridized magnon-phonon polaron, while the red and blue dashed curves represents dispersion relation of pure magnons and transverse acoustic phonons, respectively. **e** Optical setup for the time-resolved magneto-optical microscopy with the extended delay time. The excited magnetization dynamics is detected via the polarization rotation angle of the probe laser pulse induced by the magneto-optical Faraday effect in the sample. The detection is performed by an charge-coupled device (CCD) camera. **f** Magneto-optical image observed 3.5 ns after the pump pulse irradiation under the external magnetic field $B = 11.5$ mT parallel to the wavevector of the excited magnons. **g**, Wavenumber spectrum of the obtained magneto-optical images observed 3.5 ns after the excitation ($B = 11.5$ mT). The inset shows a magnified view.

pulses, we obtained temporal evolution of the spatial images of the magnetization dynamics excited by the pump pulse. We extended the maximum delay time to 35 ns by using optical fibers, so that the frequency resolution of the obtained images reaches 28 MHz, which is enough to resolve the magnon-phonon gap frequency in the sample[7,8]. All the measurements were performed at room temperature.

Observation of coherent oscillation between phonons and magnons. Figure 1f shows a spatial image of the polarization-rotation angle obtained at 3.5 ns after the pump-pulse irradiation. Vertical wave patterns appear in the vicinity of the focus of the pump pulse, demonstrating the magnon excitation by the pump pulse. By observing the sign change of the rotation caused by reversing the external magnetic field (See Supplementary Note 2), we confirmed that the polarization rotation is due mainly to the magneto-optical Faraday effect rather than the distortion-induced polarization rotation. Here, we define $\tilde{F}_\mathbf{k}(t) = \int \theta_\mathrm{F}(\mathbf{r}, t)e^{i\mathbf{kr}}d\mathbf{k}$ as the Fourier transform of the spatial image of the Faraday rotation angle with respect to the spatial coordinate. Figure 1g shows the $|\tilde{F}_\mathbf{k}(t)|^2$ at $t = 3.5$ ns. In the $k_x > 0$ region [$\mathbf{k} = (k_x, k_y)$], a region corresponding to waves propagating right in Fig. 1f, we see clear peaks of $|\tilde{F}_\mathbf{k}(t)|^2$ at $k_x = 2.93 \times 10^4$ rad·cm$^{-1} \equiv k_\mathrm{TA}$ ($k_x = 1.38 \times 10^4$ rad·cm$^{-1} \equiv k_\mathrm{LA}$) corresponding to the intersection point between magnons and TA (LA; longitudinal acoustic) phonons calculated from the parameters of LuIG. This shows that the magnon polarons are created at the intersections of the dispersion curves of magnons and phonons after the pump-pulse irradiation.

In Fig. 2a, we show the temporal evolution of the real part of $\tilde{F}_\mathbf{k}(t)$ at $|\mathbf{k}| = k_\mathrm{TA}$ and $\mathbf{k}//\mathbf{B}$. Importantly, the envelope of the $\tilde{F}_\mathbf{k}(t)$ signal clearly oscillates; the envelope amplitude decreases from $t = 15$ ns to $t = 20$ ns, while it increases from $t = 20$ ns to $t = 25$ ns up to almost the same amplitude as at $t = 15$ ns. This oscillation is in contrast to the ordinary relaxation dynamics of magnons, which monotonically decreases, but rather implies oscillation of magnon density.

In Fig. 2b, we show the frequency power spectrum of $\tilde{F}_\mathbf{k}(t)$, $F_\mathbf{k}(\omega) = \int \theta_\mathrm{F}(\mathbf{r}, t)e^{i(\mathbf{kr}-\omega t)}d\mathbf{k}dt$, at $|\mathbf{k}| = k_\mathrm{TA}$, where $\mathbf{k}//\mathbf{B}$. The frequency spectrum exhibits two peaks, suggesting the level splitting at the intersection of the magnon and TA phonon dispersion curves. The splitting width 70 MHz coincides with the inverse of the period for the observed oscillation envelope shown in Fig. 2a (14 ns), implying that the splitting is related to the observed oscillation.

When we measure pure magnons directly with the TRMO technique, we should see the periodically oscillating signal as a function of time with the frequency of magnons. Since we measure magneto-optical Faraday rotation, the signal disappears when magnons are transformed into phonons. Therefore, the observed oscillation of the signal envelope shown in Fig. 2a implies the periodic coherent beating oscillation between magnon and phonon in the time domain.

To confirm that the observed envelope oscillation is magnon-phonon beating oscillation, we examine field-angular dependence; if the observed oscillation is the beating, it should disappear for LA phonons since the magnon-phonon coupling coefficient takes minimum for LA phonons when $\mathbf{k}//\mathbf{B}$. The effective magnetic field $\mathbf{b} = (b_y, b_z)$ acting on local magnetization due to the magnon-phonon coupling can be written as[27],

$$\begin{pmatrix} b_y \\ b_z \end{pmatrix} = \begin{pmatrix} 2b_2\epsilon_{xz}\cos\theta_\mathbf{k} \\ b_1\epsilon_{xx}\sin 2\theta_\mathbf{k} \end{pmatrix}, \qquad (1)$$

where b_1 and b_2 are the magneto-elastic coupling constants, and $\theta_\mathbf{k}$ is the relative angle between the wavevector of magnons and the saturation magnetization. ϵ_{xx} and ϵ_{xz} are the elastic strain

tensor components induced by phonons. ϵ_{xx} (ϵ_{xz}) becomes nonzero for LA (TA) phonons. When $\theta_\mathbf{k} = 0$($\mathbf{k}//\mathbf{B}$), LA phonons induce minimal effective fields, while TA phonons induce maximum effective fields. On the other hand, both LA and TA phonons induce minimal effective fields when $\theta_\mathbf{k} = 90°$($\mathbf{k}\perp\mathbf{B}$). Therefore, the coherent oscillation should disappear when $k_x = k_\mathrm{LA}$($\mathbf{k}//\mathbf{B}$), $k_x = k_\mathrm{LA}$($\mathbf{k}\perp\mathbf{B}$), and $k_x = k_\mathrm{TA}$($\mathbf{k}\perp\mathbf{B}$). We show the temporal evolution of the real part of the experimentally obtained $\tilde{F}_\mathbf{k}(t)$ at $k_x = k_\mathrm{LA}$($\mathbf{k}//\mathbf{B}$) in Fig. 2d. When $\mathbf{k}//\mathbf{B}$, the envelope amplitude of the $\tilde{F}_\mathbf{k}(t)$ does not oscillate but monotonically decreases. The frequency spectrum of the $\tilde{F}_\mathbf{k}(t)$ exhibits a single peak at $k_x = k_\mathrm{LA}$($\mathbf{k}//\mathbf{B}$), as shown in Fig. 2e, consistent with the $\theta_\mathbf{k}$ dependence of the effective field representing the magnon-phonon coupling [Fig. 2f]. Figure 2g and h show the temporal evolution of $\tilde{F}_\mathbf{k}$ at $k_x = k_\mathrm{LA}$($\mathbf{k}\perp\mathbf{B}$) and $k_x = k_\mathrm{TA}$($\mathbf{k}\perp\mathbf{B}$), respectively. The envelope of $\tilde{F}_\mathbf{k}(t)$ does not oscillate in both cases, consistent with the prediction that the effective field is minimized under these conditions. We also performed measurement at $\theta_\mathbf{k} = 45°$, where the magneto-elastic coupling is maximized for LA phonon, however, we could not see clear oscillation due to large damping of magnons (See Supplementary Note 3).

To demonstrate how coherent beating oscillation is observed in real space, we show the temporal change in the wave pattern excited by the pump pulse in Fig. 2i. At $t = 15$ ns, we see clear wave pattern with the characteristic wavelength of $\lambda_\mathrm{TA} = 2\pi/k_\mathrm{TA} = 2.1$ µm, while at $t = 20$ ns, the period of the strong wave pattern changes to $\lambda_\mathrm{LA} = 2\pi/k_\mathrm{LA} = 4.6$ µm. This is because the magnon amplitude $\tilde{F}_\mathbf{k}(t)$ at $k = k_\mathrm{TA}$ decreases owing to coherent beating oscillation, while the $\tilde{F}_\mathbf{k}(t)$ at $k = k_\mathrm{LA}$ remains finite. After another 10 ns, the wave pattern of k_TA mode recovers its intensity, which are all consistent with the result shown in Fig. 2a and d.

Excitation spectra of magnons and coherent oscillation frequency. We now discuss the results in terms of the relation between magnon excitation spectra and coherent oscillation frequency. By using the effective field $\mathbf{b}$, we calculate the coherent oscillation frequency as follows (See Method),

$$\Delta f = \frac{1}{2\pi}\sqrt{\left[\omega_\mathrm{m}(k; \mathbf{B}) - \omega_\mathrm{p}(k)\right]^2 + \sigma_k^2}, \qquad (2)$$

where $\sigma_k = b_2 k\sqrt{\frac{2\gamma}{\rho M_s \omega_t}}$ is the magnon-phonon gap frequency, $\gamma = 2\pi \times 2.8 \times 10^{10}$ Hz·T^{-1} is the gyromagnetic ratio, $\rho = 7.39 \times 10^3$ kg·m^{-3} is the density of the sample, $M_s = 1.48 \times 10^4$ A·m^{-1} is the saturation magnetization, and $k = |\mathbf{k}|$ is the wavenumber. $\omega_\mathrm{m}(k; \mathbf{B})$ and $\omega_\mathrm{p}(k)$ are the angular frequency of magnons and phonons, respectively. ω_t is the angular frequency at the intersection between magnon and phonon dispersion curves. In Fig. 3a, we show a magnified view of $|F_\mathbf{k}(\omega)|^2$ near the intersection. The spectrum intensity is in good agreement with the theoretical calculation exhibiting anticrossing gap around the intersection of the dispersion curves. Figure 3b shows the oscillation frequency as a function of the wavenumber obtained from the time-domain analysis of the $\tilde{F}_\mathbf{k}(t)$. The obtained oscillation frequency exhibits a V-shaped curve which takes a minimum at the intersection point. The bottom frequency of the V-shaped curve remains finite within the error bar. The result demonstrates again the formation of the anti-crossing gap caused by the magnon-phonon coupling, which has yet to be observed in magnetic garnet films[28–30]. When the external magnetic field is increased to 13.0 mT, the spectrum peak shifts towards higher wavenumbers (Fig. 3c). The magnetic field dependence confirms that the observed gap is not due to the phonons, which do not
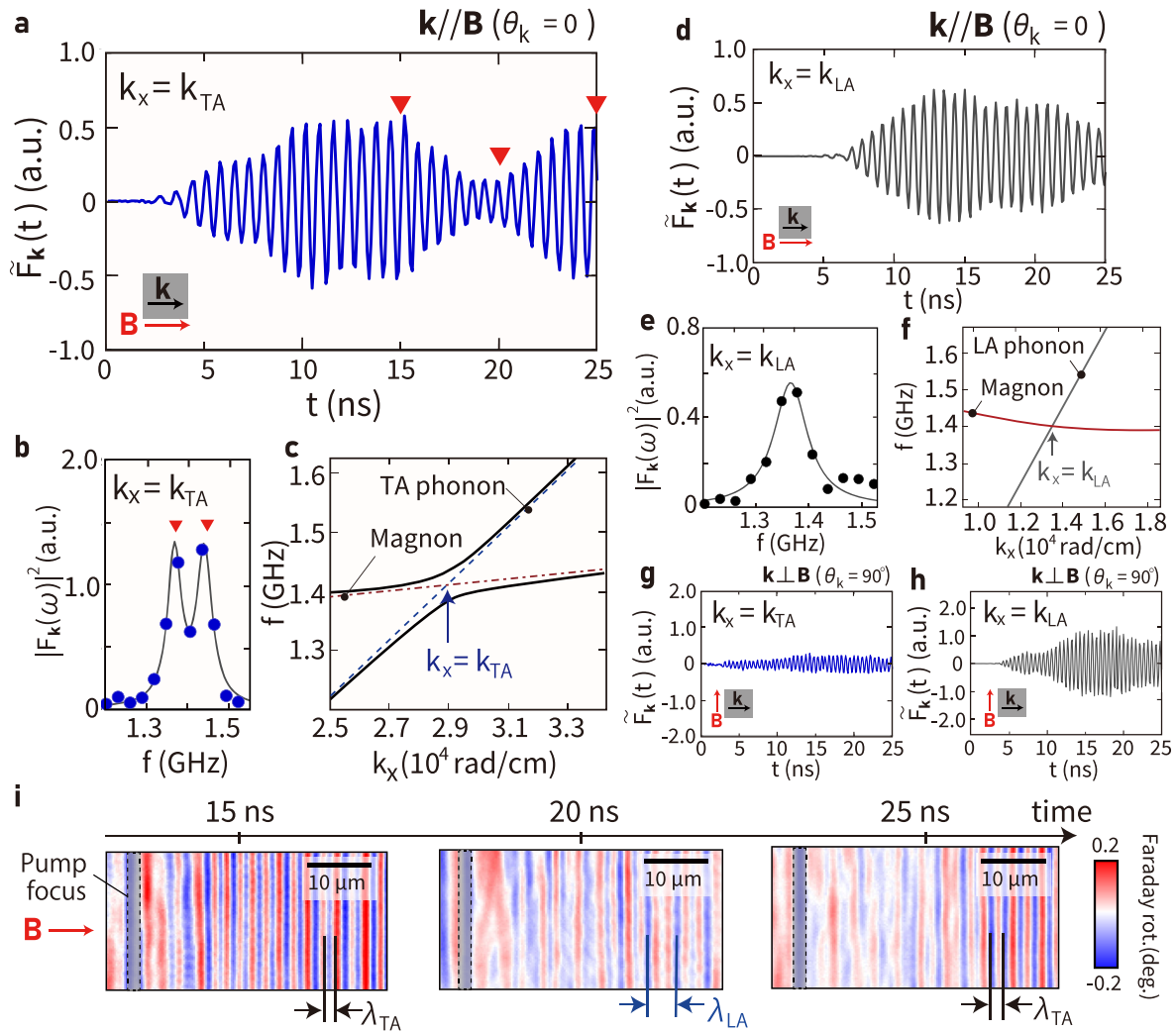
Fig. 2 Observation of magnon-phonon coherent oscillation. a Temporal evolution of the real part of $\tilde{F}_{\mathbf{k}}(t)$ at $k_x = k_{TA}$ under the magnetic field $B = 11.5$ mT parallel to $\mathbf{k}$, where k_{TA} refers to the wavenumber of the intersection point between dispersion relations of transverse acoustic (TA) phonons and magnons. Red inverted triangles indicates $t = 15$ ns, 20 ns, and 25 ns after the pump pulse irradiation. **b** A frequency power spectrum of $\tilde{F}_{\mathbf{k}}(t)$ at $k_x = k_{TA}$. The blue filled circles represents experimentally obtained spectrum intensity, while the gray curve represents fitting curve. Inverted red triangle highlights peaks. Errors of the data are evaluated as a standard deviation, which is smaller than the data plot. **c** Theoretically calculated dispersion curves of magnon polarons around $k_x = k_{TA}$ and $k_y = 0$, where we use the crystalline anisotropy energy $K_c = 73.0$ [J · m^{-3}], uniaxial anisotropy energy $K_u = -767.5$ [J · m^{-3}], saturation magnetization $M_s = 14.8$ [kA · m^{-1}], velocity of LA phonons $v_{LA} = 6.51$ [km · s^{-1}], velocity of TA phonons $v_{TA} = 3.06$ [km · s^{-1}] and magnon-phonon coupling constant $b_2 = 1.8 \times 10^5$ [J · m^{-3}]. The black solid curves represent the dispersion curves of magnon polarons, while the blue and red dashed curves represent pure TA phonons and magnons, respectively. **d** Temporal evolution of the real part of $\tilde{F}_{\mathbf{k}}(t)$ at $k_x = k_{LA}$ under the magnetic field $B = 11.5$ mT parallel to $\mathbf{k}$, where k_{LA} refers to the wavenumber of the intersection point between dispersion relations of longitudinal acoustic (LA) phonons and magnons. **e** A frequency power spectrum of $\tilde{F}_{\mathbf{k}}(t)$ at $k_x = k_{LA}$. The black filled circles represents experimentally obtained spectrum intensity, while the gray curve represents fitting curve. Errors of the data are evaluated as a standard deviation, which is smaller than the data plot. **f** Theoretically calculated dispersion curves of magnon polarons around $k_x = k_{LA}$. The gray line and red curve represent the dispersion curves of LA phonons and magnons, respectively. **g** Temporal evolution of the real part of $\tilde{F}_{\mathbf{k}}(t)$ at $k_x = k_{TA}$ under the magnetic field $B = 11.5$ mT perpendicular to $\mathbf{k}$. **h** Temporal evolution of real part of $\tilde{F}_{\mathbf{k}}(t)$ at $k_x = k_{LA}$ under the magnetic field $B = 11.5$ mT perpendicular to $\mathbf{k}$. **i**, Magneto-optical images taken at different delay times.

respond to external magnetic fields. The experimental result is well reproduced by Eq. (2), as shown in Fig. 3b and d, showing that the observed envelope oscillation of $\tilde{F}_{\mathbf{k}}(t)$ is attributed to the coherent oscillation between phonons and magnons.

Discussion

We numerically calculated the temporal evolution of the magnon amplitude $\tilde{a}_k(t)$ by calculating the Fourier transform of the spectral magnon amplitude $a_k(\omega)$[31]. We considered only the coupled dynamics between TA phonons and magnons, relevant to the observed oscillation. By considering the magnon-phonon

interaction to the lowest order, Gilbert damping, and phonon relaxation, $a_k(\omega)$ can be written as follows (See Methods),

$$a_k(\omega) = -\frac{i\sigma_k f_k g_p^{ex}/2}{\left[i(\omega_m - \omega) + \kappa_m\right]\left[i(\omega_p - \omega) + \kappa_p\right] + \sigma_k^2/4}, \quad (3)$$

where κ_m and κ_p are the relaxation constants of magnons and phonons, respectively. f_k is the external driving force for phonons, and g_p^{ex} is the coupling between phonons and f_k (See Method). ω_m and ω_p are the angular frequency of magnon and phonon at a wavenumber k, respectively. In Fig. 4a and b, we compared the experimentally obtained temporal evolution of $|\tilde{F}_{\mathbf{k}}(t)|^2$ as a
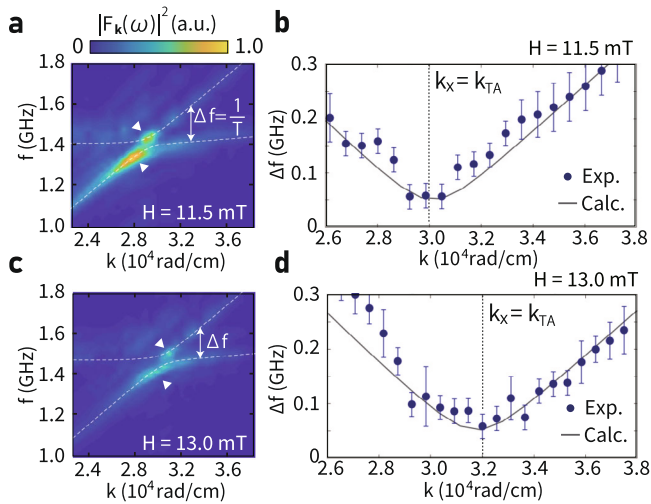
Fig. 3 Wavenumber and field dependence of magnon-phonon coherent oscillation. a Frequency spectrum $F_{\mathbf{k}}(\omega)$ observed at $B = 11.5$ mT around the intersection of the magnon and transverse acoustic (TA) phonon dispersion curves. **b** Comparison between experimentally obtained gap between the upper branch and lower branch of the spectrum at $B = 11.5$ mT and the theoretical calculation of the gap frequency. Error bars represent standard deviation. **c** Frequency spectrum $F_{\mathbf{k}}(\omega)$ observed at $B = 13.0$ mT around the intersection of the magnon and TA-phonon dispersion curves. **d** Comparison between experimentally obtained gap between the upper branch and lower branch of the frequency spectrum at $B = 13.0$ mT and the theoretical calculation of the gap frequency.
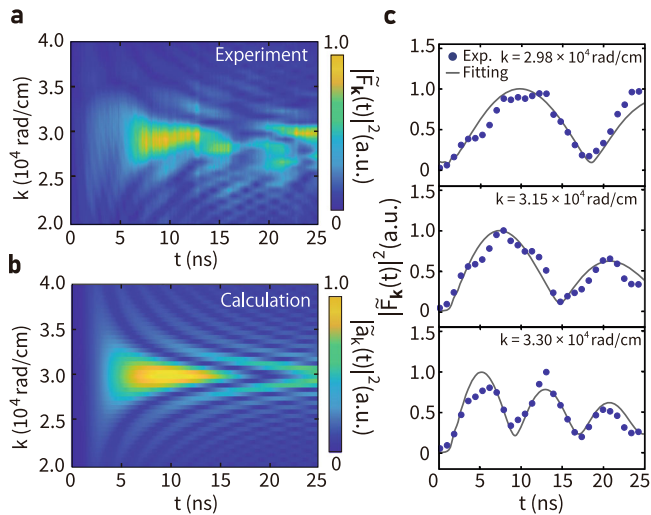
Fig. 4 Parameter fitting of coherent oscillation. a Experimentally obtained temporal evolution of $|\tilde{F}_{\mathbf{k}}(t)|^2$ at $B = 11.5$ mT. **b** Calculated temporal evolution of magnon amplitude $|\tilde{a}_{\mathbf{k}}(t)|^2$. **c** Temporal evolution of $|\tilde{F}_{\mathbf{k}}(t)|^2$ at different wavenumbers. Gray curves represents fitting curves according to Eq. (3). Errors of the data are evaluated as a standard deviation, which is smaller than the data plot.

function of the wavenumber with the calculated magnon amplitude $|\tilde{a}_{\mathbf{k}}(t)|^2$. The $|\tilde{F}_{\mathbf{k}}(t)|^2$ and $|\tilde{a}_{\mathbf{k}}(t)|^2$ exhibit similar wavenumber-dependent oscillation. We estimated the magnon-phonon gap frequency σ_k and the relaxation constants κ_m and κ_p by fitting the experimentally obtained magnon amplitude, as shown in Fig. 4c. Table 1 shows the estimated magnon-phonon coupling strength and the relaxation constants of magnons and phonons at three different wavenumbers. The magnon-phonon

Table 1 Coupling constant σ_k, relaxation constant of magnons κ_m and phonons κ_p at different wavenumbers k in the $Lu_2Bi_1Fe_{3.4}Ga_{1.6}O_{12}$ film.

k (10^4rad·cm^{-1})	σ_k (rad·MHz)	κ_m (rad·MHz)	κ_p (rad·MHz)
2.98	53.0 ± 0.01	2.10 ± 1.2	0.49 ± 0.4
3.15	54.4 ± 0.01	9.47 ± 2.5	2.51 ± 1.5
3.30	55.9 ± 0.01	3.21 ± 0.9	7.66 ± 2.4

Errors presents standard deviation.

coupling constant $b_2 = \frac{\sigma_k}{k}\sqrt{\frac{\rho M_s \omega_t}{2\gamma}}$ is estimated to be $(1.8 \pm 0.1) \times 10^5$ J·m^{-3} for all the wavenumbers, which agrees with a previous magneto-striction study[32]. At $k = 2.98 \times 10^4$ rad·cm^{-1}, σ_k is as large as 53.0 rad·MHz, while the relaxation constants of magnons and phonons are $\kappa_m = 2.10$ rad·MHz and $\kappa_p = 0.49$ rad·MHz, corresponding to the values of lifetime $\tau_m = 2.99$ μs and $\tau_p = 12.8$ μs, respectively. For all wavenumbers, σ_k is greater than κ_m and κ_p. The result shows that the gap frequency σ_k is greater than the spectrum linewidth of both phonons and magnons in the vicinity of the anti-crossing, satisfying the condition of phonon-magnon strong coupling. We calculated the cooperativity $C = \sigma_k^2/\kappa_m\kappa_p$ of the magnon-phonon coupling to evaluate the strength of the coupling in LuIG, which gives $C = 2720 \pm 2700$ for $k = 2.98 \times 10^4$ rad·cm^{-1}, $C = 125 \pm 81$ for $k = 3.15 \times 10^4$ rad·cm^{-1}, and $C = 127 \pm 53$ for $k = 3.30 \times 10^4$ rad·cm^{-1}. The cooperativity value is much greater than previously reported magnon-phonon coupling in nanomagnet[30]. The large cooperativity is attributed to the small intrinsic magnetic damping and high-quality factor of phonon in garnet crystals[33]. Although the error of the cooperativity is still large owing to the limitation of pump-probe delay time, the result implies intrinsic magnon-phonon coupling in a plane film of LuIG can be comparable with strong coupling appears in magnon-photon coupling in a cavity[31,34]. The magnon-phonon coupling in the film can be further enhanced by fabricating phononic or magnonic crystals out of the plane film[3], which may aid in the control of magnons in magnonic circuits and devices. In addition, our demonstration of the magnon-phonon coherent oscillation provides a means of studying the dynamics of coherent superposition of coupled systems, which may pave a way to coherent control of magnetic and elastic properties in various magnetic materials.

Method

Time-resolved magneto-optical microscopy. The time-resolved magneto-optical imaging method is realized by combining the time-resolved optical spectroscopy and conventional magneto-optical imaging method, which enables the observation of magnetization dynamics in samples with the spatial resolution of 750 nm and temporal resolution of 1 ps. We used a 100 fs-duration Ti; Sapphire pulse laser system with the central wavelength of 800 nm and 1 kHz repetition frequency (Coherent Inc. Astrella). Pump pulses were prepared by separating a part of the emitted laser. To prepare probe pulses, the central wavelength of a part of the emitted laser was converted to 630 nm by an optical parametric amplifier. The power of the pump and probe pulses was 1.0 μJ and 50 nJ per pulse, respectively, which was controlled by the variable ND filter. The pump and probe pulses were linearly polarized along the y-axis (Fig. 1e) by using Glan-Taylor prisms. The pump pulse was shaped into a 2.3-μm wide and ~100-μm long vertical line by using a metallic slit. An objective lens collected the transmitted probe pulse with a magnification of 20 and was then introduced to an imaging setup. The imaging setup is composed of a half-waveplate mounted on a rotation stage, an analyzer, and a charge-coupled device (CCD) camera with another objective lens of which the magnification is two. The polarization of the probe pulses was measured using the rotation analyzer method. The detailed optical configuration and analysis are shown in the Supplementary Note 2. We switch on and off the pump beam with a mechanical shutter to measure the magneto-optical images with and without the spin-wave excitation by the pump beam, and take the difference between the images. By sweeping the time delay between the pump and probe pulses, we obtained the propagation dynamics of magnons in the sample. We used an optical

fiber to extend the temporal delay between the pump and probe pulses up to 35.4 ns, of which the Fourier frequency resolution (28 MHz) corresponds to the typical energy scale of the magneto-elastic coupling[32]. We used $Lu_2Bi_1Fe_{3.4}Ga_{1.6}O_{12}$(LuIG) grown on a [001] plane of a gadolinium gallium garnet substrate by liquid phase epitaxy as a sample. LuIG is a substituted magnetic garnet with the same crystallographic structure as $Y_3Fe_5O_{12}$(YIG), which is known to exhibit small Gilbert damping. The detailed material characterization is described in Supplementary Note 1. LuIG exhibits a large magneto-optical effect (1.5 deg/μm at 630 nm) and small magnetization owing to the Ga substitution[17], leading to the small ferro-magnetic resonance (FMR) frequency. Owing to the small FMR frequency, the wavenumber of the dispersion intersection between magnons and phonons is small enough to be observed with the present TRMO microscopy. An external magnetic field was applied using a quadrupole electromagnet during the measurement. We analyzed the region in the magneto-optical image which is 10-μm away from the pump focus so as not to include the signal at the pump focus where strong non-linear effect of phonon such as structural distortion may arise. Owing to the distance between pump focus and the analyzed region, the obtained time-resolved signal has a finite time delay depending on the group velocity of the magnon polaron.

Calculation of dispersion relation of magnon polaron. In this note, we calculate the dispersion relation of magnon polaron by considering the total Hamiltonian, which involves the spin Hamiltonian, lattice Hamiltonian, and magneto-elastic coupling Hamiltonian as follows[8],

$$H_m = -\int d^3r \left(H_0 M_z + \frac{D}{2\gamma\hbar M_s} \frac{\partial M_i}{\partial x_j} \frac{\partial M_i}{\partial x_j} \right) \quad (4)$$

$$H_e = \int d^3r \left(\frac{\rho}{2} \frac{\partial u_i}{\partial t} \frac{\partial u_i}{\partial t} + \frac{\alpha}{2} \frac{\partial u_i}{\partial x_i} \frac{\partial u_j}{\partial x_j} + \frac{\beta}{2} \frac{\partial u_i}{\partial x_j} \frac{\partial u_j}{\partial x_j} \right) \quad (5)$$

$$H_{me} = \int dr^3 \frac{b_2}{2M_s^2} M_i M_j \left(\frac{\partial u_i}{\partial x_j} + \frac{\partial u_j}{\partial x_i} \right), \quad (6)$$

where, the repetitive use of indices i, j indicates summation with $i \neq j$, and H_0 is the external magnetic field, $D = 2JSa^2/\gamma\hbar$ is the exchange stiffness, γ is the gyromagnetic ratio, $\hbar$ is the Dirac constant, S is total spin, J is the exchange constant, a is the lattice constant, ρ is the density of the material, $\alpha = c_{12} + c_{44}$ and $\beta = c_{44}$ are the elastic constant, b_2 is the shear magneto-elastic constant, M_i is the i-th component of magnetization, u_i is the i-th component of displacement, M_s is the saturation magnetization, $\omega_{p\mu}(k) = v_\mu k$ is the dispersion relation of phonon with mode index μ, $v_L = \sqrt{\alpha/\rho}$, $v_T = \sqrt{\beta/2\rho}$ is the velocity of phonon, where L and T represent TA phonon and LA phonon, respectively. $\omega_m(k)$ is the dispersion relation of magnons, derived as follows by using the long-wavelength limit of B. A. Kalinikos's method[9]. In the long-wavelength limit, the dispersion relation of magnons is written as follows,

$$\omega_m(k) = \sqrt{\left(\omega_{H\beta} + \omega_M \lambda_{ex} k^2 \right) \left[\omega_{H\alpha} + \omega_M \lambda_{ex} k^2 + \omega_M \left(1 + g_k(\sin^2\theta_k - 1) + \frac{\omega_M g_k(1 - g_k)\sin^2\theta_k}{\omega_{H\alpha} + \omega_M \lambda_{ex} k^2} \right) \right]}, \quad (7)$$

where, $\lambda_{ex} = 2A_{ex}/\mu_0 M_s^2 \ [m^2]$ is the exchange constant, $\omega_M = \gamma\mu_0 M_s$, $g_k = 1 - [1 - \exp(-kd)]/(kd)$ with the sample thickness d. $\omega_{H\alpha} = \gamma\mu_0 H_\alpha$ and $\omega_{H\beta} = \gamma\mu_0 H_\beta$ is the Larmor precession frequency defined by anisotropic effective field H_α, H_β. We ignore the term originating from compressive strain because it is zero when the relative angle between θ_k is either 0 or 90°. In this case, the total effective Hamiltonian is written as follows[8],

$$H_{eff} = \sum_{k\mu} \left[\hbar\omega_m(k)\hat{a}_k^\dagger \hat{a}_k + \hbar\omega_{p\mu}(k)\hat{b}_{k\mu}^\dagger \hat{b}_{k\mu} + \frac{i}{2} \hbar\sigma_{k\mu} \left(\hat{a}_k^\dagger \hat{b}_{k\mu} - \hat{b}_{k\mu}^\dagger \hat{a}_k \right) \right], \quad (8)$$

where $\hat{a}_k(\hat{a}_k^\dagger)$ is the annihilation (creation) operator of a magnon with a wave-number k, and $b_{k\mu}(b_{k\mu}^\dagger)$ is the annihilation (creation) operator of a phonon with a wavenumber k and mode index $\mu = T, L$. $\sigma_{k\mu}$ is the coupling constant between magnon and phonon which is written as follows,

$$\sigma_{k\mu} = b_2 \sqrt{\frac{2\gamma}{\rho\omega_{p\mu}(k)M_s}}. \quad (9)$$

By diagonalizing the Hamiltonian, we obtain the following condition for the frequency of the magnon polaron ω[8],

$$(\omega^2 - \omega_p^2)(\omega - \omega_m) - \frac{1}{2}\omega_p\sigma_{k\mu}^2 = 0. \quad (10)$$

We used $\lambda_{ex} = 4.2 \times 10^{-13} \ [m^2]$, $v_L = 6.51[km \cdot s^{-1}]$, $v_T = 3.06 \ [km \cdot s^{-1}]$, $b_2 = 1.8 \times 10^5 \ [J \cdot m^{-3}]$, $\rho = 7.39 \times 10^3 \ [kg \cdot m^{-3}]$.

Derivation of coherent oscillation frequency. In this note, we derive the coherent oscillation frequency from the total effective Hamiltonian defined in the last note.

We consider the parallel magnetic field configuration where wavevector **k** and **M** are parallel. In this configuration, only the TA phonon couples with the magnons, thus we set mode index $\mu = T$. Here, we start from the effective total Hamiltonian as follows,

$$H_{eff} = \sum_k \left[\hbar\omega_m(k)\hat{a}_k^\dagger \hat{a}_k + \hbar\omega_{p\mu}(k)\hat{b}_{kT}^\dagger \hat{b}_{kT} + \frac{i}{2} \hbar\sigma_{kT} \left(\hat{a}_k^\dagger \hat{b}_{kT} - \hat{b}_{kT}^\dagger \hat{a}_k \right) \right]. \quad (11)$$

The effective Hamiltonian can be diagonalized using Bogoliubov transformation defined as follows,

$$\hat{c}_k = u_k \hat{a}_k - iv_k \hat{b}_{kT}, \quad (12)$$

$$\hat{d}_k = u_k \hat{b}_{kT} - iv_k \hat{a}_k, \quad (13)$$

where,

$$u_k = \sqrt{\frac{\omega_s + \omega_\delta}{2\omega_s}}, \quad v_k = \sqrt{\frac{\omega_s - \omega_\delta}{2\omega_s}}, \quad u_k^2 + v_k^2 = 1 \quad (14)$$

and

$$\omega_\delta = (\omega_{pT} - \omega_m)/2, \quad \omega_s = \sqrt{\omega_\delta^2 + \sigma_{kT}^2/4}. \quad (15)$$

The Bogoliubov transformation leads to the diagonalized Hamiltonian as follows,

$$H = \sum_k \left[\hbar\omega_c(k)\hat{c}_k^\dagger \hat{c}_k + \hbar\omega_d(k)\hat{d}_k^\dagger \hat{d}_k \right], \quad (16)$$

where $\omega_c(k) = (\omega_{pT} + \omega_m)/2 + \omega_s$, $\omega_c(k) = (\omega_{pT} + \omega_m)/2 - \omega_s$. Here, we define the coherent state of the hybridized wave as follows,

$$\hat{c}_k|\gamma_k\rangle = \gamma_k|\gamma_k\rangle, \quad (17)$$

$$\hat{d}_k|\delta_k\rangle = \delta_k|\delta_k\rangle, \quad (18)$$

where $\gamma_k = u_k\alpha_k - iv_k\beta_{kT}$ ($\delta_k = u_k\beta_{kT} - iv_k\alpha_k$) is the amplitude of upper (lower) branch of the magnon polaron, α_k (β_{kT}) is the amplitude of magnon (phonon), which are the eigenvalues of the coherent state $|\gamma_k\rangle, |\delta_k\rangle, |\alpha_k\rangle, |\beta_{kT}\rangle$. By using time-resolved magneto-optical microscopy, we can measure the amplitude of the magnon, which is proportional to the magnon number. The magnon number at an arbitrary time t is calculated by using the coherent state of magnon polaron, as follows,

$$\langle n_m \rangle = \langle \gamma_k, \delta_k | \hat{a}_k^\dagger(t)\hat{a}_k(t) | \gamma_k, \delta_k \rangle \quad (19)$$

$$= \langle \delta_k, \gamma_k | \left(u_k\hat{d}_k^\dagger(0)e^{i\omega_d t} + iv_k\hat{c}_k^\dagger(0)e^{i\omega_c t} \right) \left(u_k^*\hat{d}_k(0)e^{-i\omega_d t} - iv_k^*\hat{c}_k(0)e^{-i\omega_c t} \right) | \gamma_k, \delta_k \rangle \quad (20)$$
$$= |u_k|^2|\gamma_k|^2 + |v_k|^2|\delta|^2 + 2u_kv_k\gamma_k^*\delta_k|\sin(2\omega_s t + \phi),$$

where, $\tan\phi = Im(\delta_k^* \gamma_k)/Re(\delta_k^* \gamma_k)$. For an initial state, we suppose $\alpha_k = 0$, $\beta_{kT} \neq 0$ as we excite phonon predominantly by the pump pulse. Then $\gamma_k = -iv_k\beta_{kT}$, $\delta_k = u_k\beta_{kT}$ and $\phi = \pi/2$ holds, leading to the temporal evolution of magnon number as follows,

$$\langle n_m \rangle = \frac{\sigma_k^2}{2\omega_s^2}|\beta_{kT}|^2 \left[1 - \cos(2\omega_s t) \right]. \quad (21)$$

Since the frequency difference between upper and lower branch of magnon polaron is expressed by $\Delta f = \omega_c - \omega_d = 2\omega_s$, this derivation leads to the expression in Eq. (2). We plotted the Δf in Fig. 3b and d in the main part of our paper.

Numerical calculation of coherent oscillation. In this note, we derive the coherent oscillation amplitude as a function of wavenumber k and time t. We consider non-Hermitian Hamiltonian including loss of magnons and phonons, and external field under parallel configuration as follows,

$$H = \sum_k \left[\hbar\omega_m \hat{a}_k^\dagger \hat{a}_k + \hbar\omega_{pT} \hat{b}_{kT}^\dagger \hat{b}_{kT} + \frac{i\hbar}{2} \sigma_{kT} \left(\hat{a}_k^\dagger \hat{b}_{kT} - \hat{b}_{kT}^\dagger \hat{a}_k \right) \right. \left. - i\hbar\kappa_m \hat{a}_k^\dagger \hat{a}_k - i\hbar\kappa_{pT} \hat{b}_{kT}^\dagger \hat{b}_{kT} + \hbar\kappa^{ex} \left(F_k(\omega)^\dagger \hat{b}_{kT} + F_k(\omega)\hat{b}_{kT}^\dagger \right) \right], \quad (22)$$

where $\kappa_m(\kappa_{pT})$ is the damping constant of magnon (TA phonon), κ^{ex} is the coupling constant between phonon and external excitation force $F_k(\omega)$. The equation of motion of the operators leads to the following form.
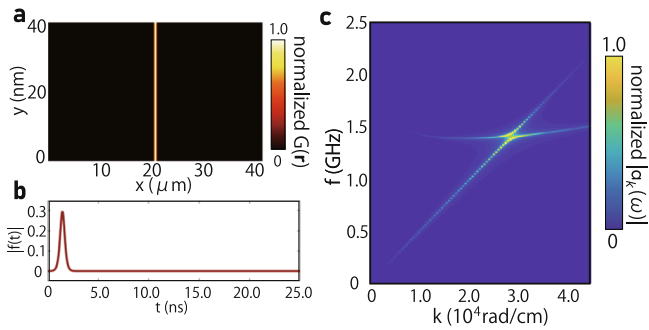
$$-i\omega\hat{a}_k = -i\omega_m\hat{a}_k - \kappa_m\hat{a}_k + \frac{\sigma_{kT}}{2}\hat{b}_{kT} \quad (23)$$

$$-i\omega\hat{b}_{kT} = -i\omega_{pT}\hat{b}_{kT} - \kappa_p\hat{b}_{kT} - i\kappa^{ex}F_k - \frac{\sigma_{kT}}{2}\hat{a}_k. \quad (24)$$

The excitation spectrum of magnons can be calculated from the equation of motion as follows,

$$\langle \hat{a}_k(\omega) \rangle = -\frac{i\sigma_k F_k g_p^{ex}/2}{[i(\omega_m - \omega) + \kappa_m] \left[i(\omega_p - \omega) + \kappa_p \right] + \sigma_{kT}^2/4}. \quad (25)$$

Here, we suppose the spectrum intensity of the external force is determined by the

Fig. 5 Numerical calculation of magnon excitation intensity. a Heat map of $G(\mathbf{r})$. σ_x and σ_y are set to realize plane-wave excitation of magnon polaron ($\sigma_x = 40$ nm, $\sigma_y = 40$ nm). **b** Time evolution of excitation intensity $f(t)$. **c** Heat map of spectrum intensity calculated according to Eq. (25) ($t_s = 1.5$ ns, $t_e = 1.6$ ns, $\sigma_t = 0.3$ ns). The spectrum intensity takes peak at the dispersion crossing between transverse acoustic (TA) phonon and magnon, reproducing the experimental results.

pump focus shape in real space[25]. Therefore the external force is expressed as follows,

$$F_{\mathbf{k}}(\omega) = \int dt d\mathbf{r}\, I_0 f(t) G(\mathbf{r}) e^{i(\mathbf{k}\mathbf{r}-\omega t)} \quad (26)$$

$$G(\mathbf{r}) = e^{-\frac{x^2}{2\sigma_x^2} - \frac{y^2}{2\sigma_y^2}} \quad (27)$$

where $\sigma_x(\sigma_y)$ is the length of the focus along $x(y)-$ axis, $\mathbf{r} = (x, y)$. The spatial distribution of the excitation intensity is plotted in Fig. 5(a). $f(t)$ is the temporal excitation function defined as follows,

$$f(t) = \tanh\frac{t-t_s}{\sigma_t} - \tanh\frac{t-t_e}{\sigma_t} + 1, \quad (28)$$

where t_s (t_e) is the start (end) time of the square-wave type excitation in time, σ_t is the parameter to describe smoothness of the square wave. The temporal evolution of the $f(t)$ is plotted in Fig. 5(b). In calculating coherent oscillation, we need only the component where $\mathbf{k} = k\mathbf{e}_x$, which is $F_k(\omega)$ since we consider parallel configuration. The calculated spectrum intensity is shown in Fig. 5(c). The intensity of the spectrum shows a peak at the crossing between dispersion relations of magnons and TA phonons as seen in the experimentally obtained excitation spectra in Fig. 3a and c.

Data availability
The data that support the findings of this study are available from the corresponding author upon reasonable request.

Code availability
The code that supports the findings of this study are available from the corresponding author upon request. All the analysis was performed by codes developed by Matlab 2017b software and Matlab signal processing toolbox.

References
1. Kajiwara, Y. et al. Transmission of electrical signals by spin-wave interconversion in a magnetic insulator. *Nature* **464**, 262–266 (2010).
2. Cornelissen, L. J., Liu, J., Duine, R. A., BenYoussef, J. & van Wees, B. J. Long-distance transport of magnon spin information in a magnetic insulator at room temperature. *NatPhys* **11**, 1022–1026 (2015).
3. Chumak, A. V., Vasyuchka, V. I., Serga, A. A. & Hillebrands, B. Magnon spintronics. *Nat. Phys.* **11**, 453–461 (2015).
4. Bauer, G. E. W., Saitoh, E. & van Wees, B. J. Spin caloritronics. *Nat. Mater.* **11**, 391–399 (2012).
5. Boona, S. R. & Heremans, J. P. Magnon thermal mean free path in yttrium iron garnet. *Phys. Rev. B* **90**, 064421 (2014).
6. Kittel, C. Interaction of Spin Waves and Ultrasonic Waves in Ferromagnetic Crystals. *Phys. Rev.* **110**, 836 (1958).
7. Rückriegel, A., Kopietz, P., Bozhko, D. A., Serga, A. A. & Hillebrands, B. Magnetoelastic modes and lifetime of magnons in thin yttrium iron garnet films. *Phys. Rev. B* **89**, 184413 (2014).
8. Guerreiro, S. C. & Rezende, S. M. Magnon-phonon interconversion in a dynamically reconfigurable magnetic material. *Phys. Rev. B* **92**, 214437 (2015).
9. Kalinikos, B. A. & Slavin, A. N. Theory of dipole-exchange spin wave spectrum for ferromagnetic films with mixed exchange boundary conditions. *J. Phys. C: Solid State Phys.* **19**, 7013 (1986).
10. Hurben, M. J. & Patton, C. E. Theory of magnetostatic waves for in-plane magnetized anisotropic films,. *J. Magn. Magn. Mat.* **163**, 39–69 (1996).
11. Bozhko, D. A. et al. Bottleneck Accumulation of Hybrid Magnetoelastic Bosons. *Phys. Rev. Lett.* **118**, 237201 (2017).
12. Hioki, T., Hashimoto, Y. & Saitoh, E. Bi-reflection of spin waves. *Commun. Phys.* **3**, 188 (2020).
13. Frey, P., Bozhko, D. A., V.S.L'vov, Hilbrands, B. & Serga, A. A. Double accumulation and anisotropic transport of magnetoelastic bosons in yttrium iron garnet films. *Phys. Rev. B* **104**, 014420 (2021).
14. Li, Y., Zhao, C., Zhang, W., Hoffmann, A. & Novosad, V. *APL Mat.* **9**, 060902 (2021).
15. Kikkawa, T. et al. Magnon Polarons in the Spin Seebeck Effect. *Phys. Rev. Lett.* **117**, 207203 (2016).
16. Flebus, B. et al. Magnon-polaron transport in magnetic insulators. *Phys. Rev. B* **95**, 144420 (2017).
17. Ramos, R. et al. Room temperature and low-field resonant enhancement of spin Seebeck effect in partially compensated magnets. *Nat. Commun.* **10**, 5162 (2019).
18. Helseth, L. E., Hansen, R. W., Il'yashenko, E. I., Baziljevich, M. & Johansen, T. H. Faraday rotation spectra of bismuth-substituted ferrite garnet films with in-plane magnetization. *Phys. Rev. B* **64**, 174406 (2001).
19. Helseth, L. E. et al. Faraday rotation and sensitivity of (100) bismuth-substituted ferrite garnet films. *Phys. Rev. B* **66**, 064405 (2002).
20. Lenk, B., Ulrichs, H., Garbs, F. & Münzenberg, M. The building blocks of magnonics. *Phys. Rep.* **507**, 107–136 (2011).
21. Au, Y. et al. Direct excitation of propagating spin waves by focused ultrashort optical pulses. *Phys. Rev. Lett.* **110**, 097201 (2013).
22. van Kampen, M. et al. All-optical probe of coherent spin waves. *Phys. Rev. Lett.* **88**, 227201 (2002).
23. Shen, K. & Bauer, G. E. W. Laser-induced spatiotemporal dynamics of magnetic films. *Phys. Rev. Lett.* **115**, 197201 (2015).
24. Hashimoto, Y. et al. Frequency and wavenumber selective excitation of spin waves through coherent energy transfer from elastic waves, Phys. Rev. B, **97**, 140404 (2018).
25. Satoh, T. et al. *Directional control spin-wave Emiss. spatially shaped light. Nat. Photon* **6**, 662–666 (2012).
26. Hashimoto, Y. et al. All-optical observation and reconstruction of spin wave dispersion. *Nat. Commun.* **8**, 15859 (2017). 140404(R) (2018).
27. Dreher, L. et al. Surface acoustic wave driven ferromagnetic resonance in nickel thin films: Theory and experiment. *Phys. Rev. B* **86**, 134415 (2012).
28. Godejohann, F. et al. Magnon polaron formed by selectively coupled coherent magnon and phonon modes of a surface patterned ferromagnet. *Phys. Rev. B* **102**, 144438 (2020).
29. Sivarajah, P. et al. THz-frequency magnon-phonon-polaritons in the collective strong-coupling regime. *J. Appl. Phys.* **125**, 213103 (2019).
30. Berk, C. et al. Strongly coupled magnon-phonon dynamics in a single nanomagnet. *Nat. Commun.* **10**, 2652 (2019).
31. Li, Y. et al. Strong Coupling between Magnons and Microwave Photons in On-Chip Ferromagnet-Superconductor Thin-Film Devices. *Phys. Rev. Lett.* **123**, 107701 (2019).
32. Nistor, I., Mayergoyz, I. D. & Rojas, R. Optical study of magnetostriction in (Bi, Ga)-substituted garnet thin films. *J. Appl. Phys.* **98**, 073901 (2005).
33. Cherepanov, V. & Kolokolov, I. V. Lavov, *Phys. Rep.* **229**(3), 81–144 (1993).
34. Zhang, X., Zou, C. L., Jiang, L. & Tang, H. X. *Phys. Rev. Lett.* **113**, 156401 (2014).

Acknowledgements

Author contributions
T.H. performed the measurement, analyzed the data, and developed the theoretical model. T.H. and E.S. planned and E.S. supervised the study. T.H. wrote the paper with review and input from Y.H. and E.S. All the authors discussed the results and explanation of the experiments.

Competing interests

The authors declare no competing interests.

Additional information